Sustainable Chemistry and Pharmacy 46 (2025) 102097

Contents lists available at ScienceDirect

Sustainable Chemistry and Pharmacy

journal homepage: www.elsevier.com/locate/scp

In depth characterization of the addition of an alumina by-product into the magnesium phosphate cementitious matrix formulated with magnesium oxide by-product

S. Huete-Hernández, J.M. Chimenos, A. Alfocea-Roig, A. Alvarez-Coscojuela, J. Giro-Paloma, J. Formosa *

Departament de Cïencia de Materials I Química Física, Universitat de Barcelona, Martí I Franquès 1-11, 08028, Barcelona, Spain

ARTICLE INFO

Handling Editor: Borhane Mahjoub

Keywords:
Magnesium phosphate cement
Low-grade magnesium oxide
Aluminum salt slag
Aluminum phosphate

ABSTRACT

This study investigates the incorporation of an alumina-rich by-product, PAVAL®, into a magnesium phosphate cement matrix formulated with low-grade magnesium oxide (LG-MgO), aiming to valorize industrial residues while improving the sustainability of chemically bonded cements. The research focuses on characterising the potential chemical interaction between aluminium species in PAVAL® and the K-struvite matrix, and evaluating whether aluminium interacts with matrix providing a better bonding.

Micromortars containing up to 35 wt% PAVAL® were prepared and characterised using XRD, FTIR-ATR, BSEM-EDS, ^{27}Al and ^{31}P MAS-NMR, and TG/DTG. The addition of PAVAL® significantly reduced the setting time from 84.5 min (0 wt% PAVAL®) to 16.5 min (35 wt% PAVAL®), which is a beneficial outcome for rapid applications, and enhanced compressive strength from 25.3 MPa (0 wt% PAVAL®) to a maximum of 40.5 MPa at 17.5 wt% PAVAL®. Although XRD and NMR did not confirm the formation of crystalline aluminophosphates, FTIR-ATR spectra showed phosphate band shifts, and BSEM-EDS mapping revealed Al-rich particles embedded within the K-struvite matrix, with signal overlap at particle boundaries.

^{31}P MAS-NMR and TGA techniques confirmed the formation of amorphous $Mg_2KH(PO_4)_2{\cdot}15H_2O$, increasing from 0.0 wt% (0 wt% PAVAL®) to 4 wt% (35 wt% PAVAL®). Concurrently, the K-struvite content decreased by 7.1 % compared with the theoretically expected amount in 35 wt% PAVAL mortars, while the $Al(OH)_3$ content also decreased by 3.5 % under the same comparison, suggesting partial solubilization and subsequent retention of aluminium as $Al(OH)_4$ through interaction with phosphate species. These findings support Al may influence the matrix through physical embedding, surface adsorption or diffusion in matrix, although the formation of defined aluminophosphates remains inconclusive under the studied conditions.

Abbreviations: **MPC**, Magnesium phosphate cement; **MKP**, Monopotassium phosphate; **MKPC**, Magnesium potassium phosphate cement; **MAPC**, Magnesium ammonium phosphate cement; **LG-MgO**, Low-grade magnesium oxide; **Sust-MPC**, Sustainable MPC; **Sust-MPC-PV**, Sustainable Magnesium phosphate cement - PAVAL® micromortars; **QF**, Quarzfin; **CART**, Citric acid reactivity test; **PV0, PV5, PV17.5, PV35**, Magnesium phosphate cement - PAVAL® micromortars formulation.

* Corresponding author.
E-mail address: joanformosa@ub.edu (J. Formosa).

https://doi.org/10.1016/j.scp.2025.102097
Received 31 March 2025; Received in revised form 21 May 2025; Accepted 21 June 2025

1. Introduction

Chemically bonded ceramics (CBCs) are inorganic solids strengthened by chemical reactions that result in chemical bonds (Wagh, 2016). Portland cement (PC), a hydraulic CBC, stands as the most extensively manufactured construction material on a global scale (Li et al., 2022), second only to concrete. Nowadays, 4.4 Gt yr^{-1} (Li et al., 2022; Survey, 2022) of PC are manufactured in the world, and this output growing annually, which carries a carbon footprint ranging from 0.81 to 0.88 tons of CO_2 emissions per metric ton of PC (Batuecas et al., 2021; Shen et al., 2016). This significant environmental impact accounts for approximately 11 % of global anthropogenic CO_2 emissions (McQueen et al., 2020) and roughly 7–8 % of world's primary energy resources (Alfocea-Roig et al., 2024; Li et al., 2022), as well as the depletion of non-renewable natural resources such as clay and limestone (Lang et al., 2025). For several decades, the scientific community has been investigating and developing alternative binders and cementitious materials with the aim of mitigating the environmental impact and replacing PC in some applications. An alternative type of CBC is magnesium phosphate cement (MPC). These cements are produced through an acid-base reaction involving MgO and phosphate salts, along with water, producing magnesium ammonium phosphate cement (MAPC) when ammonium dihydrogen phosphate ($NH_4H_2PO_4$, ADP) is used as the acid reagent, or a magnesium potassium phosphate cement (MKPC) when monopotassium phosphate (KH_2PO_4, MKP) is employed (Wagh and Jeong, 2003; Wang et al., 2024). The primary reaction products formed in this process are commonly referred to as struvite ($MgNH_4PO_4{\cdot}6H_2O$) or K-struvite ($MgKPO_4{\cdot}6H_2O$) (Ding et al., 2012; Soudée and Péra, 2000), as represented by Eqs. (1) and (2), respectively:

$$MgO_{(s)} + NH_4H_2PO_{4(s)} + 5H_2O_{(aq)} \leftrightarrows MgNH_4PO_4{\cdot}6H_2O_{(s)} \quad (1)$$

$$MgO_{(s)} + KH_2PO_{4(s)} + 5H_2O_{(aq)} \leftrightarrows MgKPO_4{\cdot}6H_2O_{(s)} \quad (2)$$

Furthermore, extensive research has demonstrated that magnesium potassium phosphate cement (MKPC), often referred to as Ceramicrete, presents several advantages when compared to magnesium ammonium phosphate cement (MAPC). These advantages include enhanced strength development, absence of ammonia volatilization, and a slower reaction rate that prolongs the setting time (Shijian and Bing, 2014), highlighting MKPC's potential as an alternative in various applications.

In terms of sustainability, the use of MgO and KH_2PO_4 as raw materials for MPCs can yield cements with a carbon footprint ranging from 0.82 to 1.32 ton of CO_2 emissions per metric ton of MPC (Shen et al., 2016; Wagh, 2016), depending on the Mg/PO_4 ratio of the binder. The carbon footprint is directly proportional to the raw materials used, with MgO accounting for 1.08–1.60 ton CO_2 emission per metric ton of cement (José et al., 2020; Shen et al., 2016; Wagh, 2016), and KH_2PO_4 contributing approximately 0.66 ton of CO_2 emission per metric ton of MPC (Wagh, 2016). Additionally, it should be noted that the carbon footprint can potentially increase due to the requirement for additional thermal treatment of MgO to reduce its reactivity and enhance the workability of the fresh MPC paste. The specific carbon footprints associated with different types of thermally treated MgO include: light burnt or caustic calcined MgO (CCM) calcined at 700–1000 °C (1.60–1.80 t CO_2 t^{-1}) (An and Xue, 2017; José et al., 2020); hard burned MgO (HBM) calcined at 1000–1400 °C (2.0–2.7 t CO_2 t^{-1}) (An and Xue, 2017; José et al., 2020); dead burned MgO (DBM) calcined at 1400–2000 °C (3.20–4.70 t CO_2 t^{-1}) (José et al., 2020; Ren et al., 2016); and fused MgO (FM) calcined at 2800 °C (10.60–12.70 t CO_2 t^{-1}) (An and Xue, 2017; José et al., 2020). Therefore, the utilization of by-products and waste materials as substitutes for the primary components in their respective functions holds great potential for significantly reducing the carbon footprint associated with the production of MPCs. These alternative materials can be regarded as having a negligible carbon footprint because they are sourced from production processes that already entail their own carbon footprint. For instance, Wagh (2016) attributes a carbon footprint of zero to the fly ash when it is added to the mixture of MgO and KH_2PO_4, forming what is known as a Ceramicrete with enhanced mechanical properties. Although Wagh's carbon footprint assessment primarily focuses on aggregates, it can also be extrapolated to encompass by-products that can replace MgO or KH_2PO_4 for the formulation of MPCs.

In particular, the use of low-grade magnesium oxide (LG-MgO) as an industrial by-product offers a highly promising approach for significant reducing the carbon footprint of MPCs. Through the complete substitution of conventional MgO in the MPC mixture, LG-MgO facilitates the development of a more sustainable MPC (Sust-MPC) (Feng et al., 2019; Formosa et al., 2008; Huete-Hernández et al., 2021; Maldonado-Alameda et al., 2017; Niubó et al., 2016). Furthermore, it is feasible to incorporate additional waste materials and by-products into the mixture, following the approach demonstrated by Wagh to enhance Ceramicrete properties (Wagh, 2016) and as the authors have previously implemented in other research by adding wool fibres (Maldonado-Alameda et al., 2023) or glass wastes (Huete-Hernández et al., 2021).

Recent research has provided evidence supporting the presence of potassium aluminum-phosphate gels in MPCs using fly ash form power plants or blast furnace slag from steel industry (Walling and Provis, 2016). This finding suggests an interaction between the aggregates and the K-struvite matrix. Moreover, recent investigations have revealed the formation of hydrated aluminum phosphate (APH) and other amorphous phases at ambient temperature in MPCs when $NH_4H_2PO_4$ is used as the phosphate source, and alumina, metakaolin, or fly ash are added as aggregates (Fan and Chen, 2015; Liu and Chen, 2016; Liu et al., 2020). Other studies have explored the utilization of a low-grade bauxite by-product, resulting in the generation of $AlPO_4$, APHs, as well as additional amorphous phases (Liu et al., 2020). Consequently, further investigation into the aluminum-phosphate reaction at room temperature holds significant interest, as this interaction could reinforce the material's structural integrity.

Whit this purpose, this study examines the addition of PAVAL® (PV) as a micro-aggregate in the formulation of Sust-MPC, a by-product obtained from the treatment of salt slag generated during the aluminum recycling process, primarily composed of alumina Al_2O_3 and $Al(OH)_3$ (Gil and Korili, 2016; Huete-Hernández et al., 2023). An interaction between the aluminum present in the PV and the K-struvite matrix is again expected, facilitating the formation aluminum phosphate hydrated phases to enhance water stability and

mechanical performance (Fan and Chen, 2015; Gardner et al., 2015; Xu et al., 2017). In this case, this process may be facilitated by the exothermic acid-base reaction (Wagh et al., 2003).

In the context of a circular economy, the use of secondary resources as precursors in the formulation of binding materials has gained attention in recent decades (Ding et al., 2024; Sertsoongnern et al., 2024; Tang et al., 2024). This is because (i) it enhances the sustainability of the construction sector and (ii) reduces the carbon footprint of the industry. The authors have previously demonstrated the feasibility of developing MPCs using secondary sources as starting material (Alfocea-Roig et al., 2023), as well as their favourable end-of-life performance in terms of ecotoxicity parameters (Muñoz-Ruiz et al., 2024). Accordingly, this research aims to develop novel Sust-MPC using low-grade magnesium oxide (LG-MgO) as magnesium source and PV as micro-aggregate, resulting in a micromortar formulation due to the inherently fine micrometric particle size of PV. The incorporation of Al-rich wastes or by-products into MPCs has previously been explored using materials such as red mud, fly ash, or metakaolin. However, the novelty of this research lies in the valorization of the PV by-product, used here for the first time in MPCs, alongside LG-MgO, which is commonly employed to formulate sustainable MPCs. Additionally, the study will evaluate the extent of interaction between PV and the K-struvite matrix, assessing whether it behaves as an inert micro-aggregate or reacts with the magnesium phosphate cement. Furthermore, a comprehensive physicochemical characterization of Sust-MPC-PV micromortars will be conducted to identify potential reaction pathway that could lead to the newformed aluminum-phosphate phases.

2. Materials and methods

2.1. Materials

LG-MgO was supplied by Magnesitas Navarras S.A. (Spain) as a by-product generated during the calcination process of natural magnesite ($MgCO_3$) to produce MgO. This by-product serves as a crucial refractory material in the steelmaking industry and finds applications in other sectors such as agriculture and livestock. Throughout the calcination process, LG-MgO is collected as a fine brown powder using the cyclone dust air pollution control system.

PV was provided by Befesa S.A. (Spain) and consists of aluminum-rich oxide and hydroxide phases (Gil, 2005; Maldonado-Alameda et al., 2021). PV arrived as a hydrated black dust and, prior to mixing the micromortars, was dried (80 °C), and milled under 80 μm to increase its surface area with the aim of promoting its reactivity. Afterward, the two by-products were individually homogenized to ensure a consistent chemical composition.

The phosphate and setting retarder used in the study were commercially available products. KH_2PO_4 was supplied by Norken S.L.

Table 1
Physicochemical characterization of the by-products used in the formulation of Sust-MPC-PV.

By-product	XRF (wt.%)											
	MgO	Al_2O_3	CaO	SiO_2	Fe_2O_3	MnO	K_2O	TiO_2	P_2O_5	Na_2O	SO_3	LOI[a]
LG-MgO	64.78	0.34	5.37	1.89	2.46	–	–	–	–	–	5.48	19.68
PV	5.01	60.85	2.70	8.00	2.60	0.25	0.76	0.72	0.11	3.11	–	15.89

	PSD d_{10} (μm)	d_{50} (μm)	d_{90} (μm)	BET ($m^2 \cdot g^{-1}$)	CART[b] (min)
LG-MgO	0.89	16.92	92.83	12.90	25.00
PV	1.16	10.29	32.99	16.02	–

XRD

By-products main crystalline phases

LG-MgO				PV			
PDF#[c]	Mineral name	Chemical formula	(wt.%)[d]	PDF#[c]	Mineral name	Chemical formula	(wt.%)[d]
01-078-0430	Periclase	MgO	50.13[e]	00-010-0173	Alumina	Al_2O_3	40.55[f]
01-071-1534	Magnesite	$MgCO_3$	21.21	00-033-0018	Gibbsite	$Al(OH)_3$	34.58
01-072-1214	Calcite	$CaCO_3$	13.70	00-024-0006	Nordstrandite	$Al(OH)_3$	
01-083-1766	Dolomite	$MgCa(CO_3)_2$	5.19	01-085-0795	Quartz	SiO_2	6.64
01-083-0114	Brucite	$Mg(OH)_2$	2.10	–	–	MgO	4.06[f]
		Others	7.66			Others	14.17
		∑	100			∑	100

[a] Loss On Ignition at 1050 °C.
[b] Citric Acid Reactivity Test.
[c] Powder Diffraction File number, from International Centre for Diffraction Data (ICDD).
[d] Estimated from the stoichiometry of decomposition reactions in TGA, combined with XRD and XRF results.
[e] Part of the MgO estimated is in the form of other compounds detected such as magnesium silicates.
[f] Part of the Al_2O_3 and MgO estimated is in the form of other compounds detected such as spinel.

(99.8 wt% of purity), and it is classified as a food-grade chemical, commonly used as a soil fertilizer. Optibor® technical grade boric acid (H_3BO_3, HB) was acquired from Borax España S.A. and was employed as the setting retarder. Moreover, Quarzfin (QF), sourced from Sibelco company ($SiO_2 > 98.5$ wt%), was added to Sust-MPC to replicate the Sust-MPC-PV micromortars, serving as an inert silica filler.

2.2. Materials characterization

The chemical composition of LG-MgO and PV was analyzed using X-ray fluorescence (XRF) with a Philips PW2400 X-ray sequential spectrophotometer. Particle size distribution (PSD) analysis was performed using a Beckman Coulter LS 13 320, and the specific surface area was determined using the BET (Brunauer, Emmett, and Teller) method, employing a Micromeritics Tristar 3000. The reactivity of LG-MgO was evaluated through the citric acid reactivity test (CART) involving acid neutralization. X-ray diffraction (XRD) analysis using a PANalytical X'Pert PRO MPD Alpha1 powder diffractometer was used to identify the main crystalline phases of the raw materials. Furthermore, thermal stability was assessed by subjecting both by-products to thermogravimetric analysis with derivative thermogravimetry (TG/DTG) using a TA Instruments Q600 SDT equipment. The determinations were conducted under a nitrogen atmosphere (50 mL min^{-1}) in the temperature range of 30–1200 °C with a heating rate of 10 °C min^{-1}. The composition of PV and LG-MgO was estimated by combining the results from XRF, XRD, and TG/DTG. The main characterization features of LG-MgO and PV are summarized in Table 1 and are detailed in depth in previous study (Huete-Hernández et al., 2023).

QF was also subjected to PSD analysis for characterization exhibiting values of 3.23 μm (d_{10}), 57.19 μm (d_{50}), and 173.5 μm (d_{90}) with a BET surface area of 0.54 m^2g^{-1}.

2.3. Sust-MPC-PV preparation

The micromortar formulations investigated in this study are summarized in Table 2 as well as setting time and compressive strength at 28 days from previous investigation (Huete-Hernández et al., 2023). For all formulations, the LG-MgO/KH_2PO_4 ratio of the cement precursors (C) was consistently set at 60/40, and the boric acid to cement ratio (HB/C) was fixed at 0.0075 both based on a previous study (Huete-Hernández et al., 2023; Niubó et al., 2016).

To prepare each micromortar sample, all solid raw materials were combined in a planetary mixer until homogeneous. Subsequently, water was added, and the mixture was further mixed for 90 s. The resulting mixtures were then poured into 40 mm × 40 mm × 160 mm expanded polystyrene prismatic moulds in triplicate and vibrated for 10 s. After 1 day, the specimens were demoulded and cured for 28 days at a temperature of 25 ± 0.5 °C and a relative humidity of 50 ± 3 % before undergoing testing.

2.4. Sust-MPC-PV characterization

2.4.1. Setting measured through isothermal conduction calorimetry (ICC)

The Isothermal Conduction Calorimetric (ICC) experiment was performed using a TA Instruments 8-channel TAM-Air instrument. The calorimeter thermostat was set at 25 °C throughout the entire experiment. In this case, batches were prepared *in situ* inside the calorimeter. Water was injected onto the solid powder using an Ad-Mix system, comprising a sealed glass ampoule equipped with a stirring rotor and a syringe for liquid injection. Data recording commenced upon the injection of water, marking the initial contact with the powder and initiating the reaction. Subsequently, the paste was mixed for 90 s, and the heat flow was recorded for 70 h. The tested formulations, as outlined in Table 3, represented the extremes, in order to evaluate the potential reaction of PV with the cement matrix of K-struvite. Additionally to PV formulations, an inert silica filler, QF, was utilized to prepare the QF35 formulation (see Table 3) for comparison with PV35. The W/C and W/S were fixed accordingly to the dosage specified in Table 2.

2.4.2. Microstructure characterization

The Sust-MPC-PV micromortars were analyzed after 28 days of curing to evaluate the potential reaction of PV with the phosphate or K-struvite matrix. Samples for microstructural characterization were prepared from mechanically tested specimens. These were crushed to a particle size of approximately 4 mm, then quartered to obtain a 100 g subsample. The subsample was subsequently milled and sieved to below 63 μm until the entire material passed through the sieve. The study employed complementary techniques,

Table 2
Sust-MPC-PV micromortars formulations studied based on previous investigation (Huete-Hernández et al., 2023).

Specimen	Micromortars proportions					Summary of previous investigation	
	S						
	PV (wt.%)	C (wt.%)	HB/C	W/C	W/S	Final setting time (min)	Compressive Strength 28d (MPa)
PV0	0.00	100.00	0.0075	0.31	0.31	84.50 ± 0.56	25.31 ± 2.47
PV5	5.00	95.00	0.0075	0.31	0.28	72.00 ± 1.07	31.40 ± 2.22
PV17.5	17.50	82.50	0.0075	0.31	0.25	29.0 ± 1.63	40.48 ± 2.50
PV35	35.00	65.00	0.0075	0.31	0.23	16.50 ± 0.49	37.71 ± 2.00

PV was incorporated into the cement precursors at concentrations of 5 wt%, 17.5 wt%, and 35 wt%, while maintaining a constant water-to-cement (W/C) ratio of 0.31 to ensure workability of the pastes, as determined through preliminary tests.

Table 3
Formulations used for the Isothermal Conduction Calorimetric (ICC) study.

Specimen	Calorimetry micromortars proportions					
	S					
	QF (wt.%)	PV (wt.%)	C (wt.%)	HB/C	W/C	W/S
PV0	0.00	0.00	100.00	0.0075	0.31	0.31
PV35	0.00	35.00	65.00	0.0075	0.31	0.23
QF35	35.00	0.00	65.00	0.0075	0.31	0.23

including XRD analysis and Fourier-transform infrared spectroscopy in attenuated total reflectance mode (FTIR-ATR) using a PerkinElmer Spectrum Two FTIR-ATR spectrometer in the range of 4000–400 cm^{-1} with an average of 32 scans and a resolution of 4 cm^{-1}. Backscattered scanning electron microscopy (BSEM) combined with energy-dispersive X-ray spectroscopy (EDS, BSEM-EDS) mapping was performed. BSEM samples were prepared by cutting the specimens with a diamond saw, followed by thorough polishing and carbon coating. EDS mapping was then performed for 20 min. Additionally, Magic Angle Spinning solid-state Nuclear Magnetic Resonance (MAS-NMR) experiments were conducted using a Bruker AVIIIHD 600 MHz spectrometer (14.09 T) at a controlled temperature of 25 °C. Cement samples (30 mg) were packed in 3.2 mm rotors and analyzed using a Cross Polarization Magic Angle Spinning (CP-MAS) probe. For ^{27}Al, the conditions included a 14 kHz spinning speed, 1 μs pulse width, 0.2 s recycling delay, and 10 000 scans. For ^{31}P, a 15 kHz spinning speed, 5 μs pulse width, 1.5 ms contact time, 3 s recycling delay, and 8000 scans were applied.

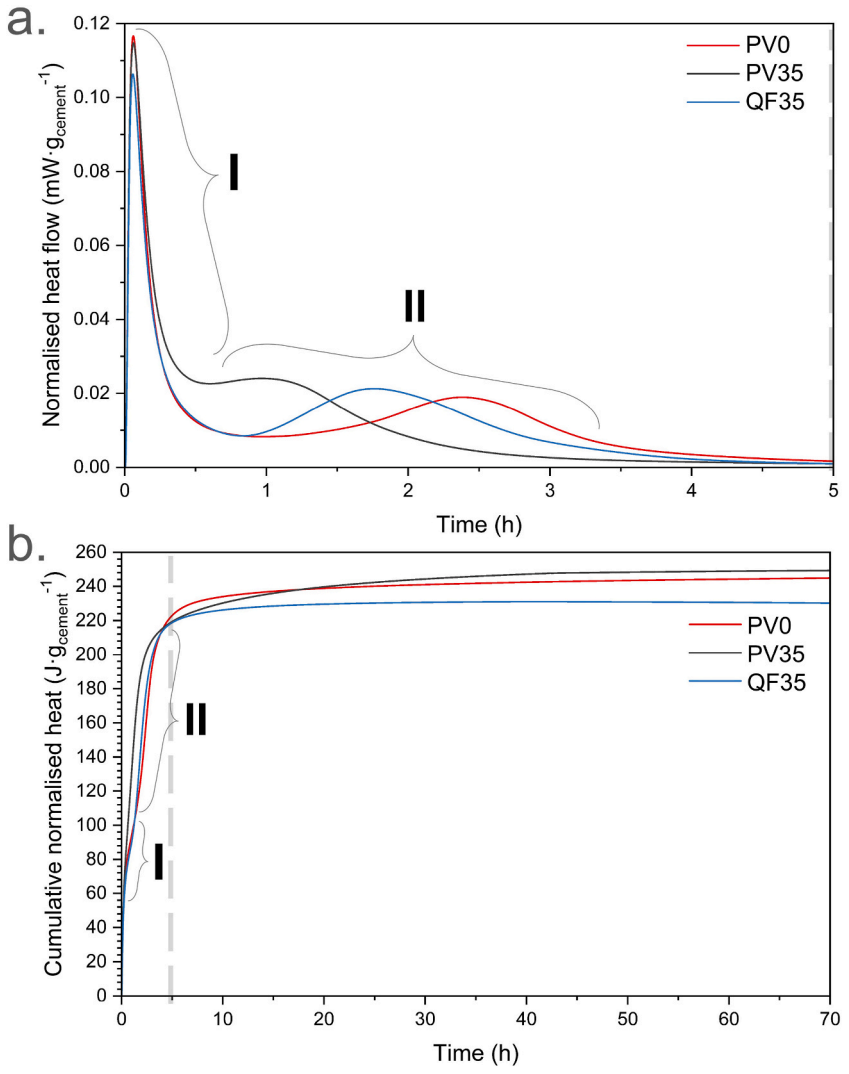

Fig. 1. Isothermal Conduction Calorimetry (ICC) of the specimens. (a) Normalized heat flow, (b) Cumulative normalized heat.

MAS-NMR was maintained at 54.74°, with chemical shifts referenced to $Al(NO_3)_3$ for ^{27}Al and $NH_4H_2PO_4$ for ^{31}P.

Furthermore, TG/DTG analysis was conducted under a nitrogen atmosphere (50 mL min^{-1}) from 30 to 1000 °C at a heating rate of 10 °C·min^{-1}.

3. Results and discussion

3.1. Sust-MPC-PV characterization

3.1.1. Isothermal Conduction Calorimetry (ICC)

The calorimetric curves in Fig. 1a depict the normalized heat flow of the micromortars during the setting reactions. The graph displays two distinct stages of the reactions. The first stage, labelled as (I), represents the dissolution of species such as Mg^{2+} and PO_4^{3-} into the aqueous slurry, as well as the hydration of species. The second stage, identified as (II), corresponds to the main reaction event, specifically involving the crystallization of K-struvite (Viani et al., 2021). Some researchers have noted multiple peaks during stage (II) and suggested that these peaks correspond to the formation of diverse amorphous structures in MPCs (Viani et al., 2021). However, in this study, only one broad peak can be observed for each formulation in stage (II), indicating the crystallization of K-struvite as previously mentioned.

The first peak, observed in stage (I), allows for the classification of PV0 as the micromortar with the highest heat flow, while QF35 exhibits the lowest heat flow. PV35 displays a higher heat flow value than expected for an inert filler. This can be mainly attributed to the potential dissolution of Al-mineral phases into the aqueous slurry, which may react with PO_4^{3-}, as well as other species present within the heterogeneity of the by-product. On the other hand, the lower heat flow observed in QF35 can be attributed to its inert nature. As for the second peak in stage (II) the maximum heat flow is reached at 1.00 h, 1.75 h and, 2.40 h for PV35, QF35 and, PV0, respectively. This indicates that PV35 exhibits the fastest crystallization of K-struvite, followed by QF35 and PV0. Hence, the addition of PV results in a reduction of the setting time, which is beneficial for repairing applications. These results align with a previous study in which an acceleration in setting time was observed (Huete-Hernández et al., 2023).

Based on the observed results, it can be asserted that both PV and QF act as accelerators of the setting reaction for MPC (Bentz et al., 2016), acting as heterogenic nucleators in the crystallization process of K-struvite. The main difference between the two lies in the notable impact of PV on enhancing the setting of MPC, primarily attributed to its smaller particle diameter and higher specific surface area, as discussed in Section 1.2 and Table 1 ($d_{50} = 10.29$ μm and 16.02 $m^2\ g^{-1}$ for PV and $d_{50} = 57.19$ μm and 0.54 $m^2\ g^{-1}$ for QF). The variation in grain size resulting from the nucleation acceleration can also be observed in Fig. 2. The ICC test was conducted for 70 h to identify and evaluate any potential reactions. No additional clear peaks were detected. However, the results of the cumulative heat release (J·g^{-1}) throughout the setting process reveal that after the completion of the last setting reaction, indicated by the discontinuous grey bar at the 5-h mark on the graph, the micromortars continued to exhibit a gradual heat release, as depicted in Fig. 1b. As expected, the micromortar displaying the least heat release after 70 h was QF35, as it contains less cement compared to PV0. Interestingly, PV35, despite sharing the same cement content as QF35 (65 wt%), exhibited the highest heat release, slightly surpassing PV0. This suggests the occurrence of further parallel reactions during the experiment involving Sust-MPC-PV micromortars. These may include the release of ammonia from the PV, able to form struvite, or the potential reaction of PV Al-species with phosphate, resulting in the formation of a reinforced K-struvite matrix, as mentioned earlier.

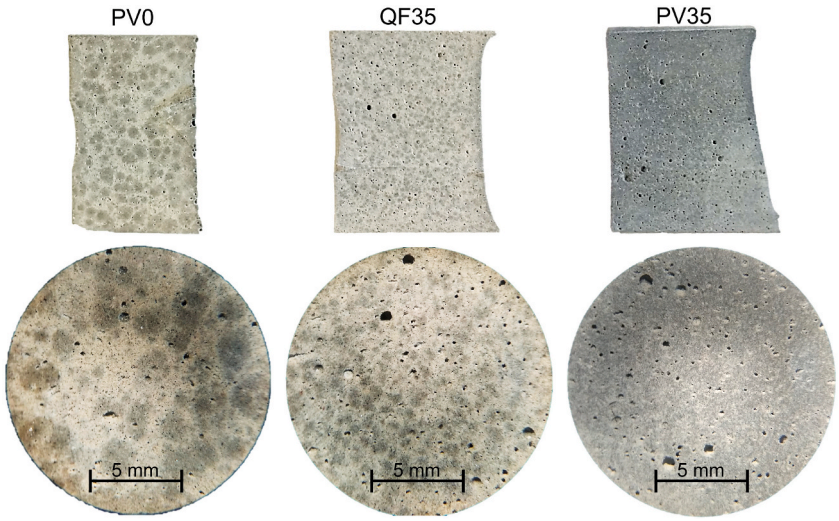

Fig. 2. Augmented images of the sections of MPC-PV Calorimetry specimens.

3.1.2. Microstructure of the micromortars

3.1.2.1. Crystalline structure (XRD). All micromortar specimens were analyzed using XRD, and the resulting patterns were thoroughly interpreted to characterize the main crystalline phases formed during curing. PV35, being the formulation with the highest PV content, was expected to exhibit more visible neoformed crystalline phases resulting from the possible interaction of PV with the cement matrix. Therefore, this study focuses on comparing PV35 and PV0. The resulting XRD pattern is shown in Fig. 3. Both PV0 and PV35 exhibited K-struvite ($KMgPO_4{\cdot}6H_2O$, PDF# 00-035-0812) as the main crystalline phase. Other crystalline phases from LG-MgO, such as magnesite, dolomite, and unreacted periclase, among others, were also present. No phosphate phases other than K-struvite were identified. PV35 showed additional phases, which originated from PV by-products. These phases include gibbsite ($Al(OH)_3$, PDF# 00-033-0018), nordstrandite ($Al(OH)_3$, PDF# 00-024-0006), and aluminum oxide (Al_2O_3, PDF# 01-075-1862), among others. Any other crystalline phases detected and not mentioned correspond to minor phases in the raw materials LG-MgO and PV.

The potential formation of $AlPO_4$ in MPCs containing aluminous materials and its hydrated forms $AlH_3(PO_4)_2{\cdot}H_2O$ and $AlH_3(PO_4)_2$ has been reported recently by other authors (Fan and Chen, 2015; Liu and Chen, 2016). Hydrated aluminum phosphates initiate the formation on the surface of alumina particles as amorphous compounds, evolving into $AlPO_4$ during the curing period (Liu et al., 2020). However, none of these phases were observed in the PV35 specimen. The pattern associated to aluminum phosphate ($AlPO_4$, PDF#01-079-2246) appeared multiple times during the characterization process but was ultimately discarded due to the low intensity of the peaks. Hence, the definitive confirmation of the presence of $AlPO_4$, $AlH_3(PO_4)_2{\cdot}H_2O$, or $AlH_3(PO_4)_2$ cannot be conclusively confirmed through XRD in this study. This uncertainty can be attributed to the low weight percentage of these components in the specimens and the heterogeneity in the crystallographic composition of the by-products, which makes the identification of minor phases challenging. This may also be attributed to the formation of amorphous aluminum phosphates or, ultimately, to the absence of their formation altogether.

3.1.2.2. Embedment of PV particles in the K-struvite matrix (BSEM). Fig. 4 shows the BSEM-EDS study of the surface of the specimen PV35. Fig. 4a provides an overall view of the surface, revealing well-dispersed particles throughout the matrix, conferring the aspect of a micromortar. Fig. 4c shows the BSEM-EDS elemental mapping of the highlighted area from Fig. 4b, while Fig. 4d illustrates the BSEM-EDS elemental mapping of Mg, Al, K, and P, respectively.

As observed, PV particles are well distributed throughout the micromortar, and the particles are embedded in the K-struvite matrix. It should be noted that the larger Al particles from PV are easily distinguishable, whereas the smaller particles are more difficult to identify in the BSEM images. When particles undergo partial reaction with the matrix, their boundaries merge with the matrix, as evident in the BSEM images. This merging of contours is visualized in the BSEM-EDS mapping images, with color changes observed at the boundaries of partially reacted particles.

This phenomenon is observed in the case of MgO particles appearing in red, with a blue contour representing P. This suggests the initial dissolution of MgO in the slurry-rich KH_2PO_4. Similarly, certain Al particles, particularly those under 10 μm, exhibit complete merging with the matrix. However, these particles cannot be detected without EDS mapping, as they are completely merged in the matrix. Mg and Al particles are also detected within the micromortar, displaying integration with the matrix and undergoing reactions. These particles are likely associated with magnesium aluminate spinel ($MgAl_2O_4$) determined from the XRD analysis of PV. Other compounds identified in the XRD characterization, such as iron oxide or magnesium carbonate, are also detected using EDS but not

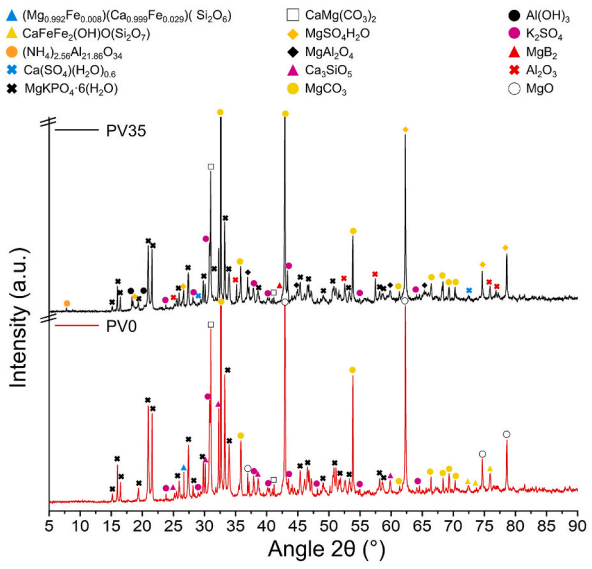

Fig. 3. XRD pattern of PV0 and PV35.

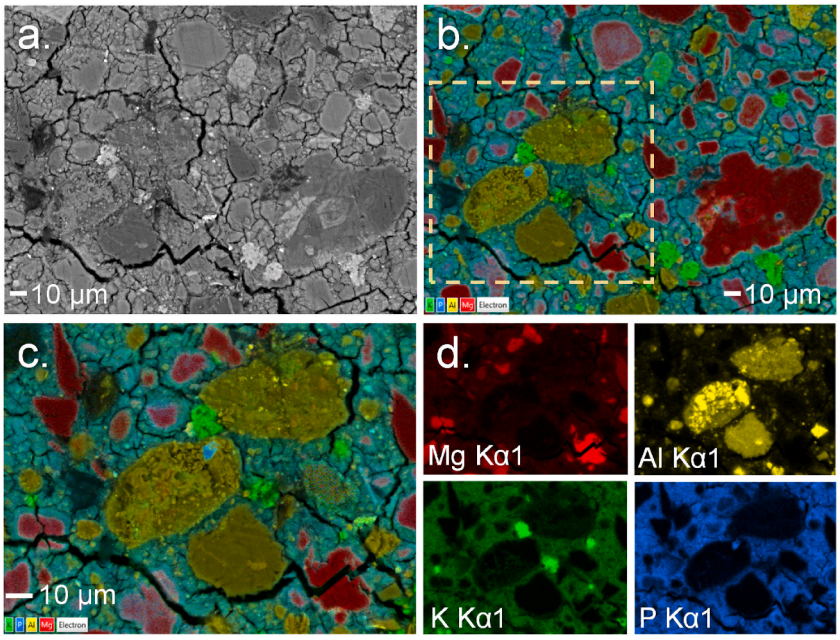

Fig. 4. BSEM-EDS Mapping of specimen PV35. (a) BSEM image, (b, c) BSEM-EDS colored combined image, (d) elemental $K_{\alpha 1}$ signal from EDS.

discussed in this manuscript. The integration of Al in the matrix is clearly visible in Fig. 5, where a fully merged Al-rich particle can be observed. This provides evidence of the high interaction between Al-rich particles from PV and the matrix within the micromortar, whether in the form of Al_2O_3 or $Al(OH)_3$. Additionally, it suggests the possible formation of aluminophosphates at the particle boundary, considering the overlap of P and K signals with the Al signal at the particle's edge, as shown in Fig. 5d.

3.1.2.3. FTIR-ATR. FTIR-ATR spectra of the PV0 and PV35 micromortars and PV is shown in Fig. 6a. In addition, the deconvolution of the phosphate characteristic region (700-1200 cm^{-1}) in Fig. 6b, c, and d for PV, PV0, and PV35, respectively. The deconvolution of the spectra was obtained by curve fitting using a Gaussian function and minimising the number of peaks. The fitting of curves was calculated by iteration until $R^2 > 0.999$. The peaks found in the micromortars in the range of 3700–2500 cm^{-1} and 2324 cm^{-1}, and 1800-1500 cm^{-1} are assigned to stretching, and bending vibrations of H–*O*–H, respectively, coming from free water and hydrated compounds like K-struvite (Man et al., 2019; Tonelli et al., 2021). The broad bands between 1500 and 1300 cm^{-1} are attributed to O–C–O asymmetrical stretching vibration (Makreski et al., 2007). The main peak of the micromortars specimens is around 1000 cm^{-1}, assigned to the primary vibrations of the phosphate (Huete-Hernández et al., 2021). PV showed a broad peak between 3700 and 3250 cm^{-1} corresponding to Al–OH (He et al., 2020). The broad peaks between 1800 and 1300 cm^{-1} correspond to water and carbonate vibrations the same way as in the micromortars. The peaks at 500 cm^{-1} correspond to Al–O vibrations from Al–O 4-coordinated (AlO_4)

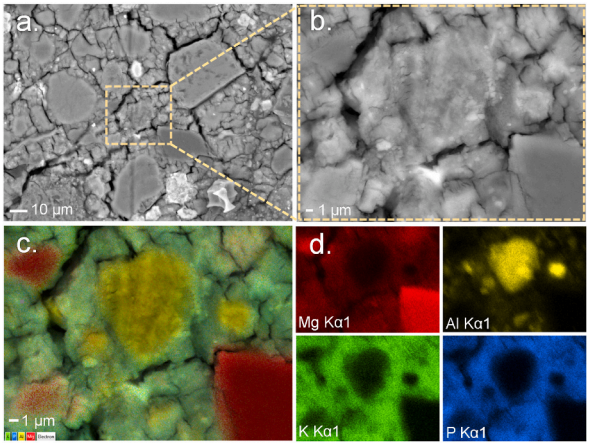

Fig. 5. BSEM-EDS Mapping of PV35 specimen. The image shows and integrated PV particle totally integrated in the K-struvite matrix. (a) BSEM image, (b) augmented zone, (c) BSEM-EDS colored combined image of the augmented zone, (d) elemental Kα1 signal from EDS.

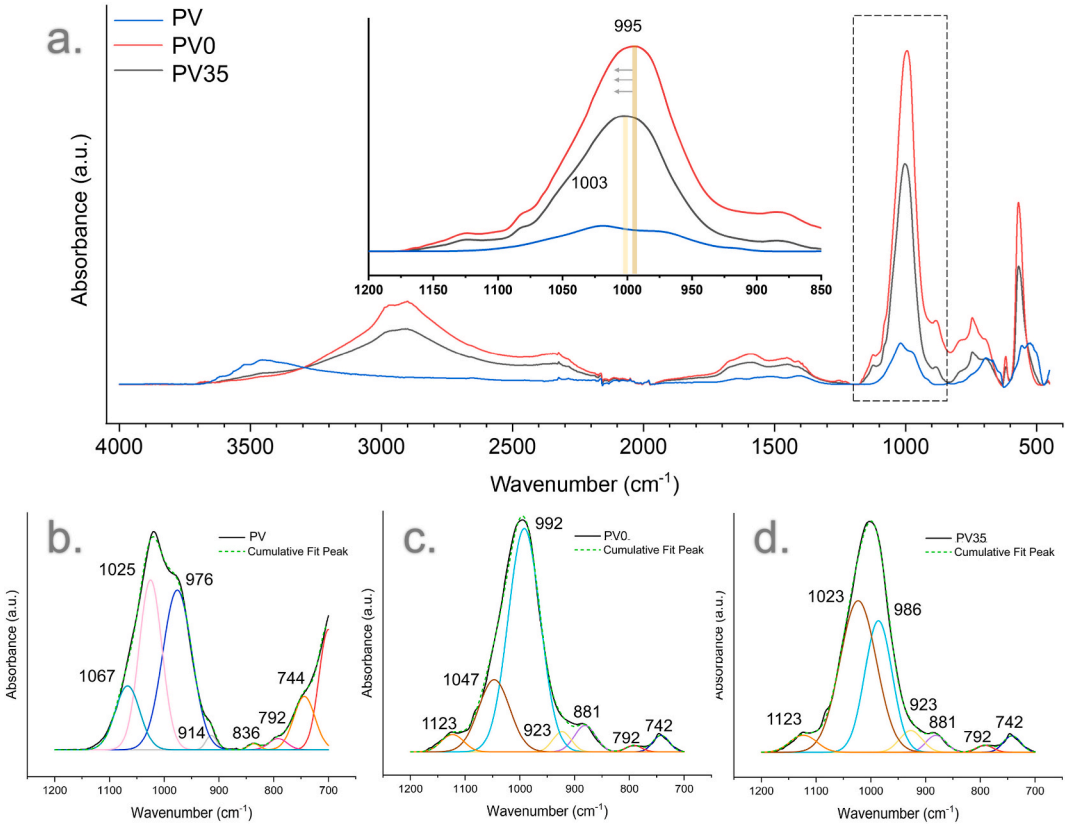

Fig. 6. PV and micromortar FTIR-ATR spectra and peak deconvolution. (a) General spectra, (b) PV spectrum deconvolution, (c) PV0 spectrum deconvolution, and (d) PV35 spectrum deconvolution.

or 6-coordinated (AlO_6) (He et al., 2020), and Al–O stretching and Al–O bonds are assigned to the band around 1000 cm^{-1} (González-Gómez et al., 2019; Li et al., 2016). The zoomed region presented in Fig. 6a reveals that the PV35 spectrum shifts towards higher frequencies, from 995 cm^{-1} (PV0) to 1003 cm^{-1} (PV35). This behavior could be related to a potential isomorphous substitution of Al in the PO_4 tetrahedron within K-struvite, or P in the AlO_4 tetrahedron within PV.

Jumping over the deconvolution zone for the PV specimen (Fig. 6b), the peaks were deconvoluted as follows: 744, 792, 836, 914, 976, 1025, and 1067 cm^{-1}, assigned to out-of-plane and in-plane bending vibrations of carbonates (Huete-Hernández et al., 2021), presence of SiO_2 (Huete-Hernández et al., 2021), stretching of Al–*O*–Al (Sayyedan and Enayati, 2019), bending vibrations of Al–OH (Yusiharni and Gilkes, 2012), stretching of AlO_4 tetrahedron (Vasconcelos et al., 2012) stretching vibration of Al–O (Li et al., 2016), and bonds of Al–O (González-Gómez et al., 2019), respectively. These results agree with the XRD results of the PV specimen. The deconvolution spectra of the micromortars resulted in 7 peaks that explained the features of the curves. Both PV0 and PV35 presented similar peaks being: 742, 792, 881, 923, 992 or 986, 1047 or 1023, and 1123 cm^{-1}. These peaks are assigned considering previous research of the authors as follows: 742 cm^{-1} to the CO_2 bending; 792 cm^{-1} to the presence of SiO_2; 881 cm^{-1} to the CO_2 bending vibration; 923 cm^{-1}, 986-992 cm^{-1}, 1023-1047 cm^{-1}, and 1123 cm^{-1} to the P–O stretching similar to the previously reported by the authors (Huete-Hernández et al., 2021). Almost all the deconvolution peaks show similarities except for the peaks at 992 (PV0) and 986 cm^{-1} (PV35), and for the peaks at 1047 (PV0) and 1023 cm^{-1} (PV35). The addition of PV induces a shift in both peaks towards lowers wavenumbers. In addition, the peak at 986 cm^{-1} shrinks mainly because of the lesser presence of phosphate in the micromortar compared to PV0. This shift towards lowers wavenumbers can indicate the potential substitution of Al in the K-struvite matrix. The longer length of the Al–O bond than that of P–O leads to lower wavenumbers. Hence, it is possible to assume that PV35 micromortar presents Al–*O*–P bonds. However, the unreacted PV that remains in the specimen could lead to an interfering interpretation of the spectrum. Another possible explanation could be that this shift is caused by the formation of amorphous hydration products, as described elsewhere in magnesium potassium phosphate cement matrices (Zhang et al., 2023).

3.1.2.4. ^{31}P and ^{27}Al MAS-NMR. In accordance with the XRD results, ^{31}P MAS-NMR (Fig. 7) confirmed the formation of K-struvite in the PV0, PV17.5, and PV35 samples, indicated by the presence of a sharp resonance at 6.5 ppm (Viani et al., 2017). The spectra for PV0 and PV17.5 did not exhibit any additional resonances. However, the PV35 spectrum displayed a broad hump-shaped peak between −5 and approximately 5 ppm, which is attributed to the formation of poorly ordered phosphate (Xu et al., 2021, 2022).

According to other publications, this could be attributed to: Cattiite ($Mg_3(PO_4)_2{\cdot}22H_2O$) at 1.1 ppm, Phosphorrösslerite

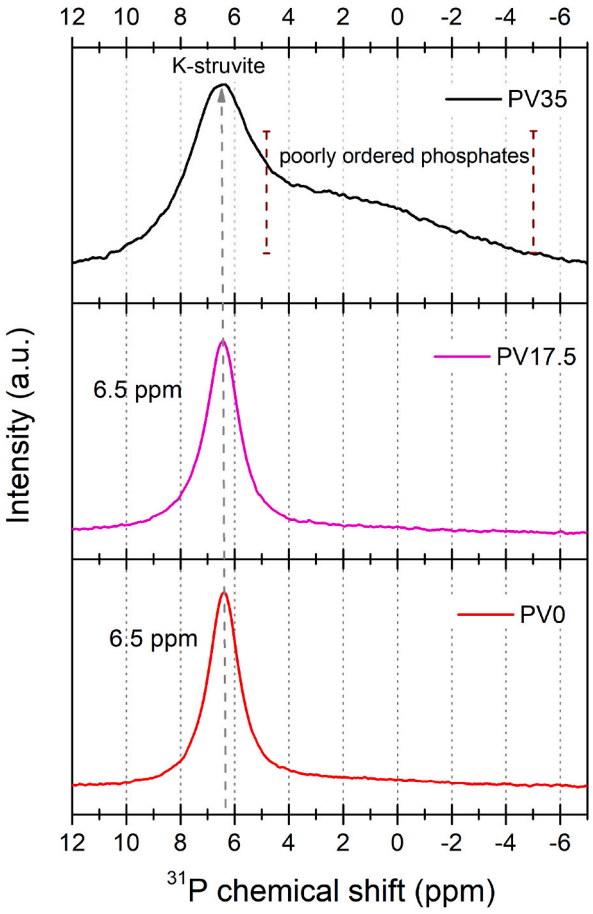

Fig. 7. ^{31}P MAS-NMR of PV0, PV17.5 and PV35.

($MgHPO_4{\cdot}7H_2O$) at 1.7 ppm, $Mg_2KH(PO_4)_2{\cdot}15H_2O$ between 2.6 ppm and 3.7 ppm, among others (Diaz Caselles et al., 2024; Lahalle et al., 2018). Determining the exact phosphate present is challenging due to the overlapping chemical shifts of various magnesium phosphates within the same spectral region, in addition to its amorphous structure which prevents its detection via XRD analysis The incorporation of PV led to the formation of a disordered phosphate within the matrix, resulting in a reduction in K-struvite formation.

The ^{27}Al MAS-NMR spectra were obtained to investigate the aluminum environment in PV0, PV17.5, PV35, and PV (Fig. 8). As

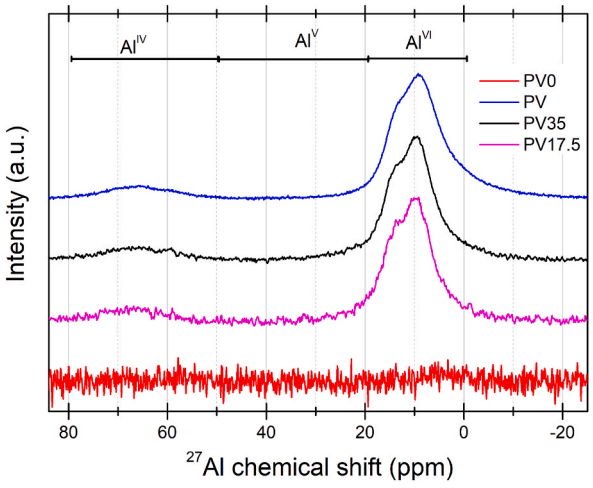

Fig. 8. ^{27}Al MAS-NMR of PV0, PV17.5, PV35, and PV.

expected, the PV0 sample showed no detectable signal due to the absence of aluminum. In contrast, the PV17.5, PV35, and PV samples exhibited resonances at 9 ppm and 70 ppm, which correspond to tetrahedrally coordinated aluminum (Al^{IV}) and octahedrally coordinated aluminum (Al^{VI}), respectively (Alvarez-Coscojuela et al., 2024; Long et al., 2024). These resonances indicate the presence of alumina and aluminum hydroxide within the PV samples, corroborating the findings from XRD analysis (Koichumanova et al., 2015; O'Dell et al., 2007). Importantly, there is no evidence to suggest the formation of $AlPO_4$ or any other interactions between aluminum and the phosphate matrix.

3.1.2.5. TG/DTG. TG/DTG thermal decomposition of the micromortars is shown in Fig. 9. The first weight loss observed around 60 °C for the PV35 sample is attributed to amorphous phosphates, such as $Mg_2KH(PO_4)_2{\cdot}15H_2O$ (Lahalle et al., 2018). It can be noted that this weight increases as PV in the mortars is incremented, thus linking the formation of amorphous phosphates to the addition of PV. This observation is in accordance with ^{31}P MAS-NMR results where the presence of phosphate salts can be observed (see Fig. 7). The second thermal decomposition around 100 °C is attributed to the loss of water of hydration from K-struvite. The third thermal decomposition, around 250 °C, is attributed to the thermal decomposition of $Al(OH)_3$. Obviously, this decomposition is only revealed in PV5, PV17.5, and PV35 micromortars, because of the inclusion of PV. The third thermal decomposition around 350 °C is due to the decomposition of $Mg(OH)_2$. The following thermal decompositions presented around 550, 650, and above 800 °C are assigned to the

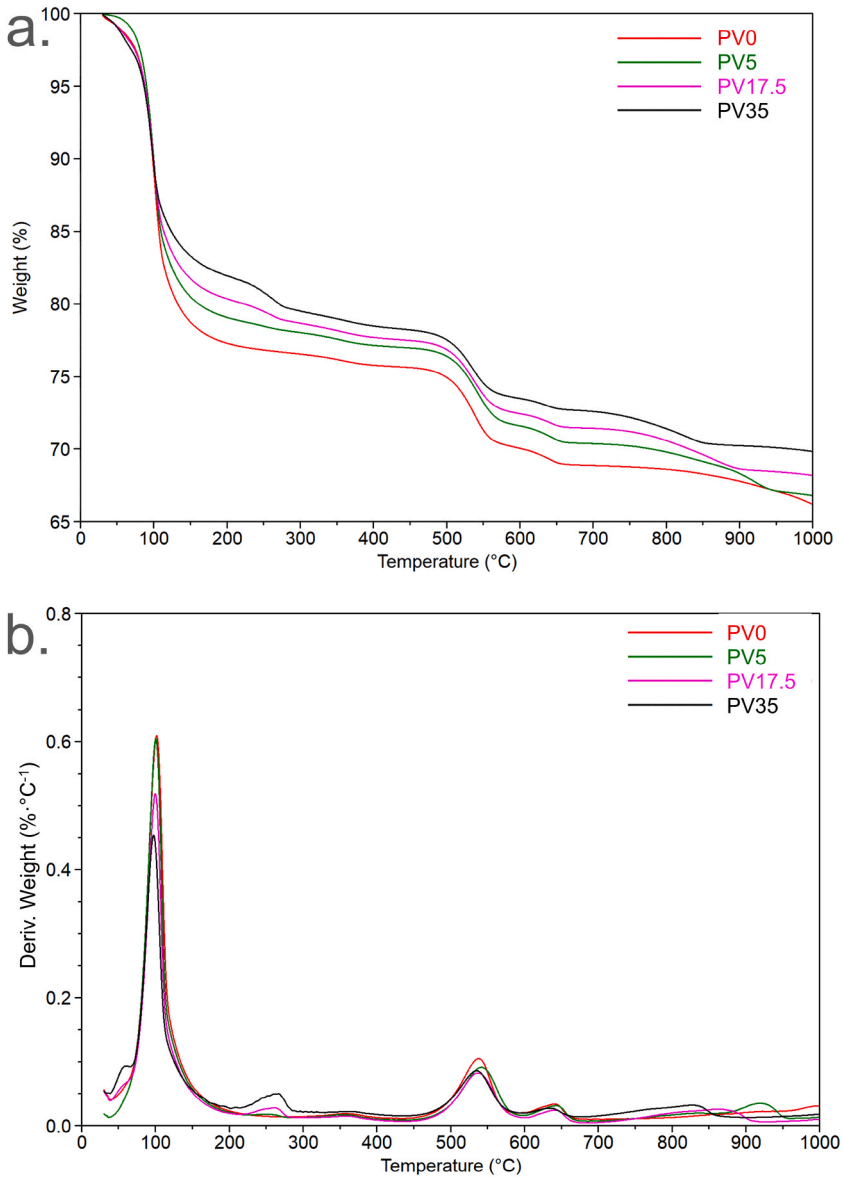

Fig. 9. TG/DTG curves of the micromortars. (a) TG signal, (b) DTG signal.

thermal decomposition of carbonates contained in LG-MgO used as precursor, in the following order: $MgCO_3$, $CaMg(CO_3)_2$, and $CaCO_3$. As it is expected, the higher the amount of PV in the micromortars, i) the lower the decomposition of K-struvite, ii) the higher the decomposition of $Al(OH)_3$, and iii) the lower the remaining residue after the experiment. To better understand the thermal decomposition behavior of the micromortars, a more detailed TGA study was conducted, focused on four distinct thermal decompositions: (i) Amorphous phosphate, like $Mg_2KH(PO_4)_2{\cdot}15H_2O$ (40–70 °C), (ii) K-struvite (70–200 °C); (iii) $Al(OH)_3$ (around 200–300 °C), which is just possible due to the presence of PV; (iv) and $CaMg(CO_3)_2$ (around 600–700 °C) as an inert phase of LG-MgO acting as a control weight loss. Therefore, this study is outlined in Table 4, encompassing TG/DTG analysis of the principal weight losses along with potential insights into the interaction between PV and MPC. This table includes (i) the corresponding TGA weight losses, (ii) the stoichiometric weight percentage in the micromortar derived from TGA based on the associated decomposition reactions, (iii) the estimation weight percentage of each compound in the micromortars based on the formulation of each micromortar, and finally, (iv) the difference between the estimation and stoichiometric TGA results. It is possible to calculate an estimation of the final amount of k-struvite, $Al(OH)_3$, and $CaMg(CO_3)_2$ in each micromortar by considering the initial formulations (Table 2). This estimation also takes into account the amount of $Al(OH)_3$ and $CaMg(CO_3)_2$ present in the composition of the raw materials (PV and LG-MgO, respectively) as shown in Table 1. Conducting TG/DTG analysis of the main weight losses offers valuable insights into the potential reaction between PV and MPC, having into account that MKP is identified as the limiting reagent. The remaining moisture in the micromortars at 28d is also considered for the calculated estimation. Although the stoichiometric result from TGA represents the actual amount of each compound in the micromortars, a comparison with the estimated value could provide insights into the interaction between PV and the K-struvite matrix. The results for dolomite decomposition reveal a good agreement, particularly for PV17.5 and PV35. The deviation values for all the micromortars consistently fall within a narrow range, approximately 0.2 wt%, which is associated with reliable TGA results and for all the calculations. However, the rest of the results indicate a tendency where the addition of PV increases the difference between the estimated and the TGA stoichiometric results. Focusing on the results of K-struvite formation in PV0 (70–200 °C) in Table 4, a difference of −6.0 wt% can be observed between the actually formed K-struvite and the estimated amount. This deviation could be attributed to the reaction yield (90.4 %), as not all the phosphate reacts, primarily due to the fast setting of the material. These observations in combination with NMR results, suggests that the decrease in the expected amount of K-struvite formation may occur due to the formation of other amorphous phosphates in contact with PV, such as $Mg_2KH(PO_4)_2{\cdot}15H_2O$. To further support this argument, an observable trend shows that the first weight loss, attributed to amorphous $Mg_2KH(PO_4)_2{\cdot}15H_2O$, increases as the PV content rises in the micromortars. These amorphous phosphates could lead to an interfering interpretation of the FTIR-ATR spectrum in the case of P–O signals, invalidating the idea of the formation of aluminophosphates in the matrix. In the case of $Al(OH)_3$, the deviation varies depending on the micromortar formulation. Specifically, in the case of PV5, the deviation is positive, indicating that the estimated amount is higher than the actual one. However, the actual and estimated amounts are close, at 1.7 and 1.4, respectively, resulting in a difference similar to that observed for dolomite as the control. For PV35, the actual $Al(OH)_3$ amount in the sample is very low compared to the estimated value. This fact could be related to the inclusion of Al from $Al(OH)_3$ into the K-struvite matrix as a leading hypothesis, reducing the amount of $Al(OH)_3$ in the sample. Al from and $Al(OH)_3$ can be slightly solubilized during matrix formation in acidic (initial stage) and alkaline (final stage) media, which may increase at setting temperatures around 60 °C (Lydersen, 1990). This slight solubilization would occur on the surface of $Al(OH)_3$ and possibly Al_2O_3-rich particles during the setting of the material provoking a formation of poor ordered phosphates on the edge of Al-rich particles. This argument is further reinforced by the observation of the fully integrated Al particle, with edges overlapping the K, P, and Mg signals from amorphous phosphates in the BSEM-EDS mappings (see Fig. 5). The dissolved Al would likely exist as $Al(OH)_4^-$ due to the alkaline medium and its tetrahedral coordination (Al^{IV}), though it is not detected by NMR because of its low concentration in the micromortar. Additionally, this could lead to an interfering interpretation of the FTIR-ATR spectrum in the case of Al–O and Al–*O*–P signals, definitively invalidating the idea of the formation of aluminophosphates in the micromortar matrix [46]

4. Conclusions

Based on the experimental work carried out to investigate the effect the addition of an alumina by-product into the magnesium phosphate cementitious matrix formulated with magnesium oxide by-product, the following conclusions can be drawn.

- The incorporation of 35 wt% PV in micromortars reduced the setting time from 2 h (for the reference cement) to 1 h, while 35 wt% QF resulted in a setting time of 1.75 h. The results demonstrated that PV can accelerate the setting process of MPC in a similar manner to the inert microaggregate QF, which is a crucial feature for repair applications.
- The observed acceleration in setting time is mainly attributed to a heterogeneous nucleation effect, potentially enhanced by the high surface area of PV. However, the relative contributions of physical versus chemical effects require further investigation, including zeta potential and surface energy analyses.
- The interaction of Al particles in PV with the phosphate in the K-struvite matrix was not clearly evidenced by XRD, FTIR-ATR, or BSEM-EDS results, although FTIR-ATR, in the range between 986 and 1023 cm^{-1}, and BSEM-EDS appeared to suggest some degree of interaction.
- NMR results indicated the presence of amorphous phosphates in the micromortars with higher PV content in the range of −5 to 5 ppm for ^{31}P chemical shift. This finding was further validated by TGA results, which attributed these phosphates primarily to amorphous $Mg_2KH(PO_4)_2{\cdot}15H_2O$ based on the mass loss detected at approximately 60 °C, forming up to 4 wt% in formulations with higher PV content. These combined results suggest that aluminum, primarily from $Al(OH)_3$ present in PV, may be slightly solubilized during the setting of the micromortar and retained as $Al(OH)_4^-$ in the outer layer of Al-rich particles. Consequently,

Table 4
TG/DTG analysis of the main weight losses focused on the interaction between PV and MPC.

Range (°C)	Decomposition reaction	Reference	Calculations (wt.%)	LG-MgO	PV	PV0	PV5	PV17.5	PV35
40–70	$Mg_2KH(PO_4)_2{\cdot}15H_2O_{(s)} \rightarrow Mg_2KH(PO_4)_{2(s)} + 15H_2O_{(g)}$	–	TGA weight loss	–	–	0.0	0.4	1.3	1.9
			TGA stoichiometric	–	–	**0.0**	**0.7**	**2.7**	**4.0**
70–200	$KMgPO_4{\cdot}6H_2O_{(s)} \rightarrow KMgPO_{4(s)} + 6H_2O_{(g)}$	**PV0**	TGA weight loss	–	–	23.0	21.6	18.8	14.8
			TGA stoichiometric	–	–	**56.6**	53.3	46.4	36.4
			Formulation estimated	–	–	**62.6**	59.5	52.9	43.4
			Difference	–	–	**−6.0**	**−6.2**	**−6.5**	**−7.1**
200–300	$2Al(OH)_{3(s)} \rightarrow Al_2O_{3(s)} + 3H_2O_{(g)}$	**PV**	TGA weight loss	–	12.0	0.0	0.6	1.4	2.4
			TGA stoichiometric	–	**34.6**	0.0	1.7	4.0	6.8
			Formulation estimated	–	**34.6**	0.0	1.4	5.0	10.3
			Difference	–	**0.0**	**0.0**	**0.3**	**−0.9**	**−3.5**
600–700	$CaMg(CO_3)_{2(s)} \rightarrow CaO_{(s)} + MgO_{(s)} + 2CO_{2(g)}$	**LG-MgO**	TGA weight loss	2.5	–	1.3	1.2	1.0	0.8
			TGA stoichiometric	**5.2**	–	2.7	2.6	2.1	1.7
			Formulation estimated	**5.2**	–	2.5	2.4	2.1	1.7
			Difference	**0.0**	–	**0.2**	**0.2**	**0.0**	**0.0**

aluminum could interfere with the formation of K-struvite at the edges of Al-rich particles, leading to the formation of amorphous phosphates in that zone. However, this remains speculative and will require further investigation due to the lack of direct evidence such as pH monitoring and ion concentration analysis. Quantitative solid-state NMR and pair distribution function (PDF) analysis could provide more evidence to differentiate the amorphous phase composition and whether if contains Al. In addition, advanced characterization techniques focused on local phase identification such as high-resolution transmission electron microscopy (HR-TEM) and synchrotron-based X-ray absorption spectroscopy (XAS) could me performed to study interface regions in future investigations.

- The formation of aluminophosphates in the micromortar matrix was not clearly evidenced by the complementary characterization techniques used in this study, ultimately not being able to validate this hypothesis.

This study highlights the potential of LG-MgO and PV industrial by-products to produce fast-setting, more sustainable MPCs with promising applicability in repair materials. The improved setting performance, combined with partial evidence of microstructural interactions, suggests that PV can play an active role beyond inert aggregate behavior.

To gain deeper insight into the reaction mechanisms and optimize material performance, future studies should include the advanced characterization abovementioned. Also, mercury intrusion porosimetry (MIP), micro-computed tomography (micro-CT), and scanning electron microscopy (SEM) of fracture surfaces would be valuable to evaluate porosity evolution and potential thermal cracking, which may have occurred due to accelerated setting. This is supported by the observed strength–setting time trade-off: PV17.5 (17.5 wt%) reached the highest strength (40.5 MPa), while PV35 (35 wt%) showed reduced strength (37.7 MPa) despite a further reduction in setting time (16.5 min). Finally, a full life cycle assessment (LCA) is needed to quantify the environmental advantages of incorporating LG-MgO and PV in MPC systems.

CRediT authorship contribution statement

S. Huete-Hernández: Writing – original draft, Investigation, Conceptualization. **J.M. Chimenos:** Writing – review & editing, Supervision, Funding acquisition. **A. Alfocea-Roig:** Writing – original draft, Investigation. **A. Alvarez-Coscojuela:** Investigation, Writing – review & editing. **J. Giro-Paloma:** Writing – review & editing. **J. Formosa:** Visualization, Funding acquisition, Writing – review & editing, Conceptualization, Supervision.

Funding

This work is supported by the Spanish Government with the Grants PID2021-125810OB-C21 funded by MCIU/AEI/10.13039/501100011033 and by "ERDF A way of making Europe". The authors would like to thank the Catalan Government for the quality accreditation and funding given to their research group DIOPMA (2021 SGR 00708). DIOPMA is a certified agent TECNIO in the category of technology developers from the Government of Catalonia. Furthermore, the Agència de Gestió d'Ajuts Universitaris i de Recerca (AGAUR) contributed through Ms A. Alfocea-Roig's PhD grant (FI-DGR, 2021). This work is also partially supported by Magnesitas Navarras, S.A. (FBG312160).

Declaration of competing interest

The authors declare that they have no known competing financial interests or personal relationships that could have appeared to influence the work reported in this paper.

Acknowledgments

The authors express their sincere gratitude to Magnesitas Navarras, S.A. for their cooperation in this research. Special appreciation is extended to the Befesa Company for providing PAVAL® and to Mr. Alberto Blanca for his assistance in conducting the experiments. Dr. Jessica Giro-Paloma is a Serra Húnter Fellow.

Data availability

Data will be made available on request.

References

Alfocea-Roig, A., Huete-Hernández, S., García-Zubiri, X., Giro-Paloma, J., Formosa, J., 2023. Can tundish deskulling waste be used as a magnesium oxide source to develop magnesium phosphate cement? J. Environ. Chem. Eng. 11. https://doi.org/10.1016/j.jece.2023.110618.

Alfocea-Roig, A., Müller, A., Steubing, B., Huete-Hernández, S., Giro-Paloma, J., Formosa, J., 2024. Life cycle assessment of the climate change impact of magnesium phosphate cements formulated with tundish deskulling waste compared to conventional cement. Sustain. Chem. Pharm. 42. https://doi.org/10.1016/j.scp.2024.101802.

Alvarez-Coscojuela, A., Mañosa, J., Formosa, J., Chimenos, J.M., 2024. Structural characterisation and reactivity measurement of chemically activated kaolinite. J. Build. Eng. 87. https://doi.org/10.1016/j.jobe.2024.109051.

An, J., Xue, X., 2017. Life-cycle carbon footprint analysis of magnesia products. Resour. Conserv. Recycl. 119, 4–11. https://doi.org/10.1016/j.resconrec.2016.09.023.

Batuecas, E., Ramón-Álvarez, I., Sánchez-Delgado, S., Torres-Carrasco, M., 2021. Carbon footprint and water use of alkali-activated and hybrid cement mortars. J. Clean. Prod. 319. https://doi.org/10.1016/j.jclepro.2021.128653.

Bentz, D.P., Zunino, F., Lootens, D., 2016. Chemical vs. Physical acceleration of cement hydration. Concr. Int. 38, 37–44.

Diaz Caselles, L., Cau Dit Coumes, C., Antonucci, P., Rousselet, A., Mesbah, A., Montouillout, V., 2024. Chemical degradation of magnesium potassium phosphate cement pastes during leaching by demineralized water: experimental investigation and modeling. Cem Concr Res 178. https://doi.org/10.1016/j.cemconres.2024.107456.

Ding, W., Wang, P., Zhao, C., He, Y., Lu, L., Wang, F., Hu, S., Zhan, Q., 2024. Study on the microstructure and impermeability of calcium aluminate cement containing metakaolin for development of high-performance marine engineering materials. Sustain. Chem. Pharm. 42. https://doi.org/10.1016/j.scp.2024.101746.

Ding, Z., Dong, B., Xing, F., Han, N., Li, Z., 2012. Cementing mechanism of potassium phosphate based magnesium phosphate cement. Ceram. Int. 38, 6281–6288. https://doi.org/10.1016/j.ceramint.2012.04.083.

Fan, S., Chen, B., 2015. Experimental research of water stability of magnesium alumina phosphate cements mortar. Constr. Build. Mater. 94, 164–171. https://doi.org/10.1016/j.conbuildmat.2015.06.050.

Feng, L., Chen, X. qing, Wen, X. dong, Zhang, ya, Z., Shou, L. yan, 2019. Investigating and optimizing the mix proportion of sustainable phosphate-based rapid repairing material. Constr. Build. Mater. 204, 550–561. https://doi.org/10.1016/j.conbuildmat.2019.01.195.

Formosa, J., Aranda, M.A., Chimenos, J.M., Rosell, J.R., Fernández, A.I., Ginés, O., 2008. Cementos químicos formulados con subproductos de óxido de magnesio. Bol. Soc. Espanola Ceram. Vidr. 47, 293–297. https://doi.org/10.3989/cyv.2008.v47.i5.169.

Gardner, L.J., Bernal, S.A., Walling, S.A., Corkhill, C.L., Provis, J.L., Hyatt, N.C., 2015. Characterisation of magnesium potassium phosphate cements blended with fly ash and ground granulated blast furnace slag. Cem Concr Res 74, 78–87. https://doi.org/10.1016/j.cemconres.2015.01.015.

Gil, A., 2005. Management of the salt cake from secondary aluminum fusion processes. Ind. Eng. Chem. Res. 44, 8852–8857. https://doi.org/10.1021/ie050835o.

Gil, A., Korili, S.A., 2016. Management and valorization of aluminum saline slags: Current status and future trends. Chem. Eng. J. 289, 74–84. https://doi.org/10.1016/j.cej.2015.12.069.

González-Gómez, M.A., Belderbos, S., Yañez-Vilar, S., Piñeiro, Y., Cleeren, F., Bormans, G., Deroose, C.M., Gsell, W., Himmelreich, U., Rivas, J., 2019. Development of superparamagnetic nanoparticles coated with polyacrylic acid and aluminum hydroxide as an efficient contrast agent for multimodal imaging. Nanomaterials 9, 1–20. https://doi.org/10.3390/nano9111626.

He, F., Li, W., Yang, L., Zhu, Z., Zhou, L., Zhang, X., He, X., 2020. Alumina aerogels with unidirectional channels under different freezing temperatures during freeze casting—Part I: control and analysis of pore channels. Ceram. Int. 46, 13588–13598. https://doi.org/10.1016/j.ceramint.2020.02.144.

Huete-Hernández, S., Maldonado-Alameda, A., Alfocea-Roig, A., Giro-Paloma, J., Chimenos, J.M., Formosa, J., 2023. Sustainable magnesium phosphate micromortars formulated with PAVAL® alumina by-product as micro-aggregate. Bol. Soc. Espanola Ceram. Vidr. 1–15. https://doi.org/10.1016/j.bsecv.2023.02.001.

Huete-Hernández, S., Maldonado-Alameda, A., Giro-Paloma, J., Chimenos, J.M., Formosa, J., 2021. Fabrication of sustainable magnesium phosphate cement micromortar using design of experiments statistical modelling: valorization of ceramic-stone-porcelain containing waste as filler. Ceram. Int. 47, 10905–10917. https://doi.org/10.1016/j.ceramint.2020.12.210.

José, N., Ahmed, H., Miguel, B., Luís, E., Jorge, de B., 2020. Magnesia (MgO) production and characterization, and its influence on the performance of cementitious materials: a review. Materials 13, 1–31. https://doi.org/10.3390/ma13214752.

Koichumanova, K., Sai Sankar Gupta, K.B., Lefferts, L., Mojet, B.L., Seshan, K., 2015. An in situ ATR-IR spectroscopy study of aluminas under aqueous phase reforming conditions. Phys. Chem. Chem. Phys. 17, 23795–23804. https://doi.org/10.1039/c5cp02168e.

Lahalle, H., Cau Dit Coumes, C., Mercier, C., Lambertin, D., Cannes, C., Delpech, S., Gauffinet, S., 2018. Influence of the w/c ratio on the hydration process of a magnesium phosphate cement and on its retardation by boric acid. Cem Concr Res 109, 159–174. https://doi.org/10.1016/j.cemconres.2018.04.010.

Lang, L., Zhu, M., Pu, S., 2025. Recycling engineering sediment waste as sustainable subgrade material using ground granulated blast-furnace slag, electrolytic manganese residue and cement. Environ. Technol. Innov. 37, 103969. https://doi.org/10.1016/j.eti.2024.103969.

Li, J., Zhao, T., Li, F., Zong, B., Du, Z., Zeng, J., 2016. A comparative study on the synthesis mechanism and microstructural development of hierarchical porous mullite monoliths obtained by the sol-gel process with three different silicon sources. Ceram. Int. 42, 4806–4818. https://doi.org/10.1016/j.ceramint.2015.11.166.

Li, Q., Su, A., Gao, X., 2022. Preparation of durable magnesium oxysulfate cement with the incorporation of mineral admixtures and sequestration of carbon dioxide. Sci. Total Environ. 809, 152127. https://doi.org/10.1016/j.scitotenv.2021.152127.

Liu, N., Chen, B., 2016. Experimental research on magnesium phosphate cements containing alumina. Constr. Build. Mater. 121, 354–360. https://doi.org/10.1016/j.conbuildmat.2016.06.010.

Liu, Y., Qin, Z., Chen, B., 2020. Influence of low-grade bauxite on the properties of magnesium phosphate cement. Constr. Build. Mater. 242, 118052. https://doi.org/10.1016/j.conbuildmat.2020.118052.

Long, S., Li, Y., Wang, N., Wang, Z., Lin, H., 2024. Research on the influence of ultrafine metakaolin on the properties of magnesium phosphate cement prepared by natural brucite. Constr. Build. Mater. 452. https://doi.org/10.1016/j.conbuildmat.2024.138952.

Lydersen, E., 1990. The solubility and hydrolysis of aqueous aluminium hydroxides in dilute fresh waters at different temperatures. Nord. Hydrol 21, 195–204. https://doi.org/10.2166/nh.1990.0015.

Makreski, P., Jovanovski, G., Kaitner, B., Gajović, A., Biljan, T., 2007. Minerals from Macedonia: IX. Distinction between some rhombohedral carbonates by FT IR spectroscopy. Vib. Spectrosc. 44, 162–170. https://doi.org/10.1016/j.vibspec.2006.11.003.

Maldonado-Alameda, A., Alfocea-Roig, A., Huete-Hernández, S., Giro-Paloma, J., Chimenos, J.M., Formosa, J., 2023. Magnesium phosphate cement incorporating sheep wool fibre for thermal insulation applications. J. Build. Eng. 76, 107043. https://doi.org/10.1016/j.jobe.2023.107043.
Maldonado-Alameda, A., Lacasta, A.M., Giro-Paloma, J., Chimenos, J.M., Haurie, L., Formosa, J., 2017. Magnesium phosphate cements formulated with low grade magnesium oxide incorporating phase change materials for thermal energy storage. Constr. Build. Mater. 155, 209–216. https://doi.org/10.1016/j.conbuildmat.2017.07.227.
Maldonado-Alameda, A., Mañosa, J., Giro-Paloma, J., Formosa, J., Chimenos, J.M., 2021. Alkali-Activated binders using bottom ash from waste-to-energy plants and aluminium recycling waste. Applied Sciences. https://doi.org/10.3390/app11093840.
Man, X., Haque, M.A., Chen, B., 2019. Engineering properties and microstructure analysis of magnesium phosphate cement mortar containing bentonite clay. Constr. Build. Mater. 227, 116656. https://doi.org/10.1016/j.conbuildmat.2019.08.037.
McQueen, N., Kelemen, P., Dipple, G., Renforth, P., Wilcox, J., 2020. Ambient weathering of magnesium oxide for CO_2 removal from air. Nat. Commun. 11, 1–10. https://doi.org/10.1038/s41467-020-16510-3.
Muñoz-Ruiz, V., Cifrian, E., Alfocea-Roig, A., Santos, J., Formosa, J., Chimenos, J.M., Andres, A., 2024. Ecotoxicity assessment of sustainable magnesium phosphate cements (Sust-MPCs) using luminescent bacteria and sea urchin embryo-larval development tests. J. Environ. Chem. Eng. 12. https://doi.org/10.1016/j.jece.2024.113995.
Niubó, M., Formosa, J., Maldonado-Alameda, A., del Valle-Zermeño, R., Chimenos, J.M., 2016. Magnesium phosphate cement formulated with low grade magnesium oxide with controlled porosity and low thermal conductivity as a function of admixture. Ceram. Int. 42, 15049–15056. https://doi.org/10.1016/j.ceramint.2016.06.159.
O'Dell, L.A., Savin, S.L.P., Chadwick, A.V., Smith, M.E., 2007. A ^{27}Al MAS NMR study of a sol-gel produced alumina: identification of the NMR parameters of the θ-Al_2O_3 transition alumina phase. Solid State Nucl. Magn. Reson. 31, 169–173. https://doi.org/10.1016/j.ssnmr.2007.05.002.
Ren, W., Xue, B., Lu, C., Zhang, Z., Zhang, Y., Jiang, L., 2016. Evaluation of GHG emissions from the production of magnesia refractory raw materials in Dashiqiao, China. J. Clean. Prod. 135, 214–222. https://doi.org/10.1016/j.jclepro.2016.06.118.
Sayyedan, F.S., Enayati, M.H., 2019. On structure and oxidation behaviour of non-stoichiometric amorphous aluminium phosphate coating. Surf. Eng. 35, 670–676. https://doi.org/10.1080/02670844.2018.1560912.
Sertsoongnern, P., Ayawanna, J., Kingnoi, N., Chaiyaput, S., 2024. Utilization of asphalt waste dust with fly ash in mixed cement materials for sustainable construction. Sustain. Chem. Pharm. 41. https://doi.org/10.1016/j.scp.2024.101699.
Shen, W., Cao, L., Li, Q., Wen, Z., Wang, J., Liu, Y., Dong, R., Tan, Y., Chen, R., 2016. Is magnesia cement low carbon? Life cycle carbon footprint comparing with Portland cement. J. Clean. Prod. 131, 20–27. https://doi.org/10.1016/j.jclepro.2016.05.082.
Shijian, F., Bing, C., 2014. Experimental study of phosphate salts influencing properties of magnesium phosphate cement. Constr. Build. Mater. 65, 480–486. https://doi.org/10.1016/j.conbuildmat.2014.05.021.
Soudée, E., Péra, J., 2000. Mechanism of setting reaction in magnesia-phosphate cements. Cem Concr Res 30, 315–321. https://doi.org/10.1016/S0008-8846(99)00254-9.
Survey, U.S.G., 2022. Mineral commodity summaries 2022. Angew. Chem. Int. Ed. 6 (11), 951–952. https://doi.org/10.3133/mcs2022.
Tang, L., He, Z., Yang, R., Pei, S., Zou, M., Qin, M., 2024. High temperature calcined red mud-cement mortar: workability, mechanical properties, hydration mechanism, and microstructure. Sustain. Chem. Pharm. 41. https://doi.org/10.1016/j.scp.2024.101717.
Tonelli, M., Gelli, R., Ridi, F., Baglioni, P., 2021. Magnesium phosphate-based cements containing Halloysite nanotubes for cracks repair. Constr. Build. Mater. 301, 124056. https://doi.org/10.1016/j.conbuildmat.2021.124056.
Vasconcelos, D.C.L., Nunes, E.H.M., Vasconcelos, W.L., 2012. AES and FTIR characterization of sol-gel alumina films. J. Non-Cryst. Solids 358, 1374–1379. https://doi.org/10.1016/j.jnoncrysol.2012.03.017.
Viani, A., Mácová, P., Sotiriadis, K., 2021. Amorphous-crystalline transformation control on the microstructural evolution of magnesium phosphate cements. Mater. Lett. 292, 129630. https://doi.org/10.1016/j.matlet.2021.129630.
Viani, A., Mali, G., Mácová, P., 2017. Investigation of amorphous and crystalline phosphates in magnesium phosphate ceramics with solid-state ^{1}H and ^{31}P NMR spectroscopy. Ceram. Int. 43, 6571–6579. https://doi.org/10.1016/j.ceramint.2017.02.087.
Wagh, A.S., 2016. Chemically bonded phosphate ceramics: twenty-first century materials with diverse applications. Chemically Bonded Phosphate Ceramics: Twenty-First Century Materials with Diverse Applications: Second Edition, second ed. Elsevier Ltd, Oxford, UK. https://doi.org/10.1016/C2014-0-02562-2.
Wagh, A.S., Grover, S., Jeong, S.Y., 2003. Chemically bonded phosphate ceramics : II , warm-temperature process for alumina. Ceramics 49, 1845–1849.
Wagh, A.S., Jeong, S.Y., 2003. Chemically bonded phosphate ceramics: I , A dissolution model of formation. J. Am. Ceram. Soc. 86, 1838–1844. https://doi.org/10.1111/j.1151-2916.2003.tb03569.x.
Walling, S.A., Provis, J.L., 2016. Magnesia-based cements: a journey of 150 Years, and cements for the future? Chem Rev 116, 4170–4204. https://doi.org/10.1021/acs.chemrev.5b00463.
Wang, D., Yue, Y., Qian, J., 2024. Effect of carbonation on the corrosion behavior of steel rebar embedded in magnesium phosphate cement. Compos. B Eng. 268. https://doi.org/10.1016/j.compositesb.2023.111088.
Xu, B., Ma, H., Shao, H., Li, Z., Lothenbach, B., 2017. Influence of fly ash on the compressive strength and micro-characteristics of magnesium potassium phosphate cement mortars. Cem Concr Res 99, 86–94. https://doi.org/10.1016/j.cemconres.2017.05.008.
Xu, B., Winnefeld, F., Lothenbach, B., 2021. Effect of temperature curing on properties and hydration of wollastonite blended magnesium potassium phosphate cements. Cem Concr Res 142, 106370. https://doi.org/10.1016/j.cemconres.2021.106370.
Xu, B., Winnefeld, F., Ma, B., Rentsch, D., Lothenbach, B., 2022. Influence of aluminum sulfate on properties and hydration of magnesium potassium phosphate cements. Cem Concr Res 156, 106788. https://doi.org/10.1016/j.cemconres.2022.106788.
Yusiharni, E., Gilkes, R., 2012. Rehydration of heated gibbsite, kaolinite and goethite: an assessment of properties and environmental significance. Appl. Clay Sci. 64, 61–74. https://doi.org/10.1016/j.clay.2011.12.005.
Zhang, G., Wang, Q., Li, Y., Zhang, M., 2023. Microstructure and micromechanical properties of magnesium phosphate cement. Cem Concr Res 172, 107227. https://doi.org/10.1016/j.cemconres.2023.107227.